analytical chemistry

Article

Cite This: Anal. Chem. 2020, 92, 1470−1476

pubs.acs.org/ac

ZIF-8-Assisted NaYF4:Yb,Tm@ZnO Converter with Exonuclease III-Powered DNA Walker for Near-Infrared Light Responsive Biosensor

Shuzhen Lv, Kangyao Zhang, Ling Zhu, and Dianping Tang*

Key Laboratory of Analytical Science for Food Safety and Biology (MOE & Fujian Province), Department of Chemistry, Fuzhou University, Fuzhou 350108, People's Republic of China

Supporting Information

ABSTRACT: This work reports a ZIF-8 (ZIF: Zeolitic Imidazolate Framework)-assisted $NaYF_4$:Yb,Tm@ZnO upconverter for the photoelectrochemical (PEC) biosensing of carcinoembryonic antigen (CEA) under near-infrared (NIR) irradiation on a homemade 3D-printed device with DNA walker-based amplification strategy. The composite photosensitive material $NaYF_4$:Yb,Tm@ZnO, as converter to transfer NIR import to photocurrent output, was driven from annealed $NaYF_4$:Yb,Tm@ZIF-8. Yb^{3+} and Tm^{3+}-codoped $NaYF_4$ ($NaYF_4$:Yb,Tm) converted NIR excitation into UV emission, matching with the absorption of ZnO for in situ excitation to generate the photocurrent. Upon target CEA introduction, the swing arm of DNA walker including the sequence of CEA aptamer carried out the sandwiched bioassembly with CEA capture aptamer on the G-rich anchorage DNA tracks-functionalized magnetic beads. Thereafter, DNA walker was triggered, and the swing arm DNA was captured by the G-rich anchorage DNA according to partly complementary pairing and Exonuclease III (Exo III) consumed anchorage DNA by a burnt-bridge mechanism to go into the next cycle. The released guanine (G) bases from DNA walker enhanced the photocurrent response on a miniature homemade 3D-printed device consisting of the detection cell, dark box, and light platform. Under optimal conditions, $NaYF_4$:Yb,Tm@ZnO-based NIR light-driven PEC biosensor presented high sensitivity and selectivity for CEA sensing with a detection limit of 0.032 ng mL^{-1}. Importantly, our strategy provides a new horizon for the development of NIR-based PEC biosensors in the aspect of developing MOF-derived photoelectric materials, flexible design of a 3D-printed device, and effective signal amplification mode.

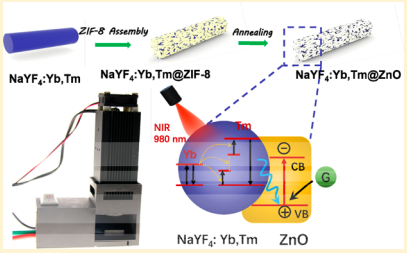

Photon upconversion of rare earth-ion-doped nanomaterials, characterized by the continuous absorption of multiple low-energy near-infrared (NIR) photons prior to emission of high energy luminescence such as ultraviolet (UV), visible (vis), or NIR light through a nonlinear optical process, has aroused wide research interest.[1−3] These overwhelming characteristics of upconversion nanoparticles (UCNPs) including low photo damage, stable chemical composition as well as large antiStokes shift have made them perfect candidates for particular applications such as, but not limited to, medical imaging, biosensing, and photoactivated therapy.[4−7] Favorably, the UCNPs-based photoelectrochemical (PEC) biosensors substitute infrared source for ultraviolet and visible light source to indirectly excite photosensitive materials as well as maintain strong penetration depth and near-zero photobleaching possessing the superiority of cost effectiveness, fast response, and high sensitivity for detection of cancer biomarkers.[8−10] However, traditional PEC sensing devices are increasingly difficult to meet the requirement of researchers for portable and flexible detection. With the development of 3D-printing technology, various 3D-printed devices have been designed. Recently, our group designed dual-channel PEC ratiometric aptasensor by using the spatial-resolved technique on a homemade 3D-printed device.[11] Nevertheless, miniature and exquisite devices still need to enhance the integration and majorization.

Metal−organic frameworks (MOFs), thanks to the abundant multiplicity in structure and composition, have attracted extensive attention. Recently, controlling growth of MOF on upconversion nanocrystals for NIR-enhanced photoelectric performance has been explored. MOFs with photoelectric properties spontaneously assembling on the surface of the UCNPs could be activated by UV/visible photons from the up-conversion luminescence of UCNPs upon NIR light excitation. For example, Li's group presented a uniform core−shell structure of $NaYF_4$:Yb,Tm@MIL-53-NH_2(Fe) NPs, where $NaYF_4$:Yb,Tm could simultaneously emit the UV and blue light for MIL-53-NH_2(Fe) in suit excitation and photocatalysis.[12] Promisingly, integrating UCNPs with MOFs would be a good inspiration for UCNPs-based PEC biosensor. As is well-known, the photosensitive materials employed in PEC biosensors are characterized by good conductivity, stability, and low electron−hole recombination rate. However, the poor electrical conductivity and bad water stability are still great challenges for the application of MOFs in electrochemical biosensors. So, the nanomaterials deriving from MOFs with tailored chemical compositions and complex architectures for the electrochemical energy storage and

Received: October 15, 2019
Accepted: November 25, 2019
Published: November 25, 2019

DOI: 10.1021/acs.analchem.9b04710
Anal. Chem. 2020, 92, 1470−1476

biosensor have come to the fore.[13−16] Lou's group developed a MOF-assisted strategy for the preparation of hierarchical hybrid Fe_2O_3@Co_3O_4 nanostructure via MIL-88B@ZIF-67 composites with enhanced lithium storage properties.[17] Wu et al. reported the fabrication of 3D hollows

CoS@PCP/CNTs, through the synchronous decomposition and sulfidation of preformed Co-based ZIF-67, is a template for high-performance lithium-ion batteries.[18] Compared with templates of these nanostructures, they had better stability, conductivity, and energy storage properties. Therefore, the preparation of photosensitive material deriving from MOFs is a promising choice for the construction of UCNPs-based PEC biosensors. Zeolitic Imidazolate Framework (ZIF), assigned to a subclass of MOFs, is crystalline tridimensional architecture comprising of metal clusters or metal ions bridged tetrahedrally by the imidazolate linker.[19] Zeolitic imidazolate framework-8 [ZIF-8, $Zn(MeIM)_2$, MeIM = 2-methylimidazole] as one of the most widely explored ZIF has been applicable to gas separation, biosensing, and drug delivery.[20−23] So far, UCNPs@ZIF-8 as template for construction of UCNPs@ZnO for PEC biosensors has not been reported.

Recently, various artificial molecular machines inspired by living systems and assembled with molecular components can achieve quasi-mechanical movements in response to a particular stimulus. DNA walking devices as the popular members of molecular machines precisely possess mechanical movement on a nanoscale objective along the designated track.[24,25] The spontaneous movements of DNA walkers are usually driven by nicking enzymes, exonuclease, strand exchange reactions, as well as photoactivated reactions.[26] Most DNA walkers with three-dimensional (3D) DNA tracks possess powerful DNA enrichment ability, playing the role of signal amplification in different biosensors for sensitivity owing to relatively large surface area. Zhang and his co-worker reported a DNA walker that was activated by a target protein on the surface of the DNA-functionalized AuNP tracks achieving signal amplification.[27] Fan's group developed a stochastic DNA walker driven by Exonuclease III autonomously moving on a spherical nucleic acid−based 3D track.[28] The powerful enrichment ability of 3D DNA tracks have accomplished great signal enhancement.

In this work, a MOF-assisted UCNPs-based PEC biosensor is proposed for CEA detection by coupling with a DNA walker on the 3D tracks for signal amplification with a homemade 3D printed device. The $NaYF_4$:Yb,Tm plays the role of light converter, in which the NIR excitation is converted into UV emission. The $NaYF_4$:Yb,Tm@ZnO composite photosensitive materials derived from annealed $NaYF_4$:Yb,Tm@ZIF-8 are excited by UV light according to $NaYF_4$:Yb,Tm for in situ absorption of zinc oxide (ZnO) to generate photocurrent under 980 nm illumination. As shown in Scheme 1 and Supporting Information (SI) Figure S1, the sandwich-type bioassembly consisting of aptamer-CEA-aptamer is carried out on the biofunctionalized magnetic bead according to biotin−streptavidin recognition where hundreds of single-stranded DNA as anchors constructed the 3D DNA tracks. Specifically, once the target CEA is introduced into the detection system, the swing arm of DNA walker containing the sequence of CEA aptamer is combined with the compounds of CEA-capture aptamer and then captured by G-rich anchorage DNA according to partly complementary pairing at the other end. The DNA walker moves autonomously via consuming G-rich anchorage DNA with Exo III through a burnt-bridge

Scheme 1. Schematic Illustration of ZIF-8-Assisted $NaYF_4$:Yb,Tm@ZnO Upconverter with Exonuclease III-Powered DNA Walker for CEA Detection Under 980 nm Illumination on a Homemade 3D-Printed Device

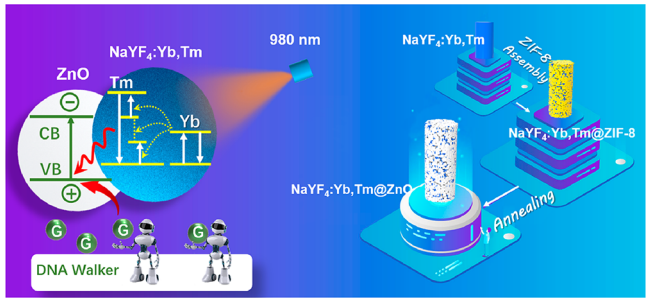

mechanism (catalytic removal of anchorage DNA from the blunt 3′ termini) to release guanine (G) bases, inhibiting electron−hole recombination, thus resulting in the enhancement of photocurrent. To surmount target-independent spontaneous hybridization between anchorage DNA and swing arm DNA, the blocker DNA, which is complementary to one segment of the swing arm, was designed. The complementary sequences between the swing arm DNA and blocker DNA are longer than those of the swing arm DNA and anchorage DNA. In this case, the swing arm DNA cannot combine the anchorage DNA in the absence of target analyte. Upon addition of target CEA, the blocker DNA is initially removed via Exo III, and then the released swing arm executes the next process of DNA walker. Finally, the 3D-printed device containing detection cell, dark box, and light platform is designed for developing portable and miniature photocurrent testing.

EXPERIMENTAL SECTION

Preparation of Photoactive $NaYF_4$:Yb,Tm@ZIF-8 and $NaYF_4$:Yb,Tm@ZnO Materials. First, oleic acid (OA) ligands on the surface of $NaYF_4$:Yb,Tm was removed to provide a suitable surface for the assembly of ZIF-8.[12] Specifically, 0.2 mmol of OA-capped $NaYF_4$:Yb,Tm was dispersed into 15 mL of ethanol with ultrasonic treatment, followed by adding 1.2 mL HCl (35 wt %) for 30 min washing. Subsequently, $NaYF_4$:Yb,Tm was collected from the mixture by centrifugation (5500*g*,10 min). To further remove residual OA ligands from $NaYF_4$:Yb,Tm surface, the precipitate was put into another ethanol solution containing HCl (pH 4) for another 10 min ultrasonic washing (twice). After that, $NaYF_4$:Yb,Tm was dispersed into 35 mL ethanol containing the PVP (0.035 g, Mw = 24 000) to form a PVP layer on the surface of the $NaYF_4$:Yb,Tm. The product was obtained by centrifugation and then washed with ethanol thoroughly after magnetically stirring overnight.

A layer-by-layer growing mode was carried out for the ZIF-8 self-assembly on $NaYF_4$:Yb,Tm surface. First, 0.2 mmol of PVP-coated $NaYF_4$:Yb,Tm and 0.05 mmol of $Zn(NO_3)_2{\cdot}6H_2O$ were dispersed in methanol (30 mL). After the solution was stirred for 40 min for Zn^{2+} absorption, 0.183 mmol of 2-methylimidazole was added to the mixture and reacted for 3 h. Then, the intermediate product was obtained by centrifugation (5500*g*, 10 min) and the same growing process was repeated twice to increase the ZIF-8 thickness. After that, the resulting $NaYF_4$:Yb,Tm@ZIF-8 product was washed with ethanol by centrifugation (5500*g*, 10 min). Finally, $NaYF_4$:Yb,Tm@ZIF-8

DOI: 10.1021/acs.analchem.9b04710
Anal. Chem. 2020, 92, 1470−1476

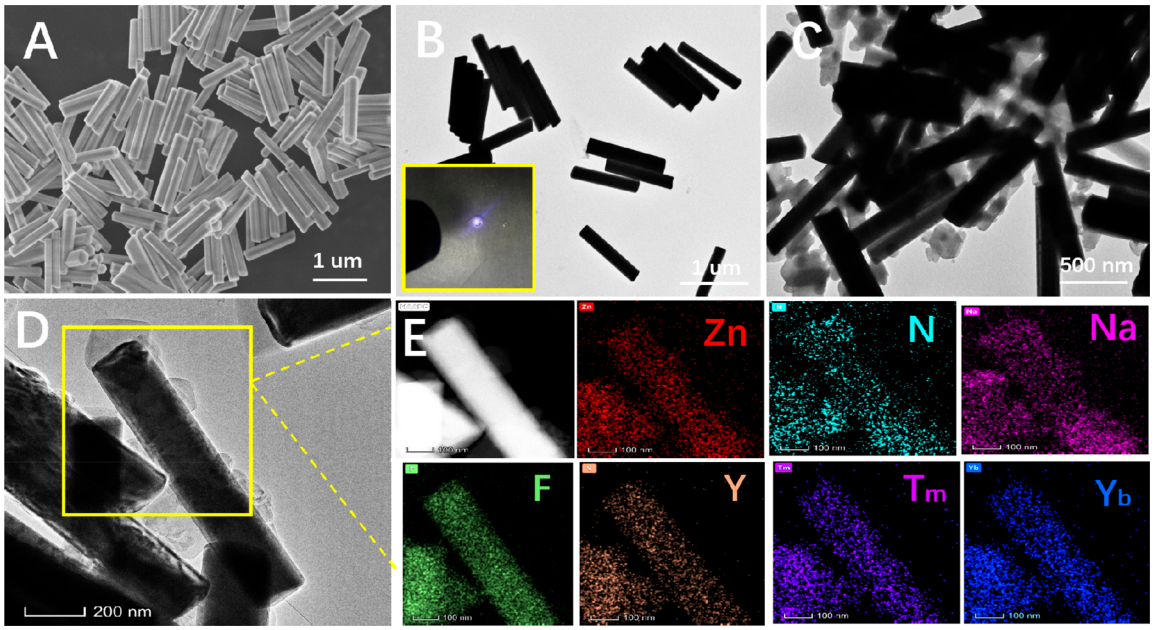

Figure 1. (A) SEM and (B) TEM images of $NaYF_4$:Yb,Tm (insert: upconversion photoluminescence of $NaYF_4$:Yb,Tm upon NIR excitation at 980 nm); TEM images of (C, D) $NaYF_4$:Yb,Tm@ZIF-8 microrods and corresponding HAADF-STEM image and element mappings (E) for Zn (red), N (wathet blue), Na (pink), F (green), Y (orange), Tm (purple), and Yb (mazarine blue).

was calcined at 350 °C for 90 min, and then the temperature was increased to 400 °C (~60 min) for the generation of the $NaYF_4$:Yb,Tm@ZnO.[29]

Construction of DNA 3D Tracks on Magnetic Beads. The purchased streptavidin-modified magnetic beads were coated with biotin-anchorage DNA and biotin-CEA capture aptamer according to the previous literature with minor modification.[30] First, 2.5 μL of streptavidin-modified magnetic beads (initial concentration) were washed with TTL buffer (100 mM Tris, 0.1% Tween-20, 1.0 M LiCl, pH 8.0) and dispersed in TE buffer (10 mM Tris and 1.0 mM Na_2EDTA, pH 9.0). Then the mixture including 50-μL biotin-CEA capture aptamer as well as 50-μL biotin-anchorage DNA at a molar ratio of 1:100 was dropped into streptavidin-modified magnetic beads suspension and incubated for 120 min at room temperature. The final product was washed twice by magnetic separation to remove redundant DNA, dispersed in 500-μL PBS buffer (pH 7.4) and stored at 4 °C when not in use.

Fabrication of NIR Light-Mediated PEC Biosensor and Photocurrent Measurement. Prior to the detection of target CEA, the swing arm DNA (100 μM) first hybridized with the blocker DNA (100 μM) to avoid the target-independent spontaneous hybridization. Then, the CEA target with various concentrations were added into 300 μL of as-prepared DNA-functionalized magnetic beads. After incubation for 60 min at 37 °C with slight shaking, the mixture was added into PBS solution (10 mM, pH 7.4) containing blocked swing arm DNA (50 μM) for another 60 min incubation at 37 °C. Following that, the mixture was magnetically separated, washed with PBS, and redispersed in a 200 μL reaction buffer (10 mM Tris-HCl, 10 mM KCl, pH 7.0) containing Exo III (15 U). The reaction time of the DNA walker assisted by Exo III was 110 min for digesting the G-rich anchorage DNA and releasing individual guanine bases. Then, the released guanine bases was dropped into the detection cell for photocurrent measurement.

Prior to detection, the gold printed electrode with a length of 37 mm, a width of 10 mm, and a thickness of 0.8 mm was coated with $NaYF_4$:Yb,Tm@ZnO (6.0 mg mL^{-1}) after cleaning with ethanol. As shown in SI Figure S2 and Figure 3D, six parts constituted the miniature 3D printed PEC detection device which was printed with the black photosensitive resin material. The gold electrode was put into the printed cuboid miniature detection cell (including part 6: an injection layer, part 5: a circulation layer, and part 4: an electrode placement layer) which was fixed on the groove of the printed black box (part 1). The top of the printed miniature black box could put the NIR laser (2.0 W, 980 nm) for the excitation of the $NaYF_4$:Yb,Tm@ZnO. The switch of the NIR laser was set on another printed dark box (part 2) which could control the time to turn on the light. After the above reaction solution and Na_2SO_4 (0.2 M) solution were injected into the detection cell, part 3 was installed on part 1 playing the role of shielding function to exclude the interference of external light. The PEC detection was carried out on an AutoLab electrochemical workstation using the $i-t$ curve method.

RESULTS AND DISCUSSION

Characterization of ZIF-8-Assisted $NaYF_4$:Yb,Tm@ZnO. The microstructure and morphology of the prepared $NaYF_4$:Yb,Tm were characterized via scanning electron microscopy (SEM) and transmission electron microscopy (TEM). As depicted in Figure 1A,B, $NaYF_4$:Yb,Tm displayed a uniform rod-like shape with the diameter of about 200 nm along their entire length which were up to 1.0−1.2 μm. Moreover, the pure $NaYF_4$:Yb,Tm microrods with smooth surface could emit blue violet light upon the NIR laser irradiation (insert in Figure 1B), indicating the successful preparation of the $NaYF_4$:Yb,Tm microrods. In this strategy, the successful assembly of ZIF-8 onto $NaYF_4$:Yb,Tm microrods was significant due to the fact that $NaYF_4$:Yb,Tm@ZnO as the composite photosensitive material originated from the

DOI: 10.1021/acs.analchem.9b04710
Anal. Chem. 2020, 92, 1470−1476

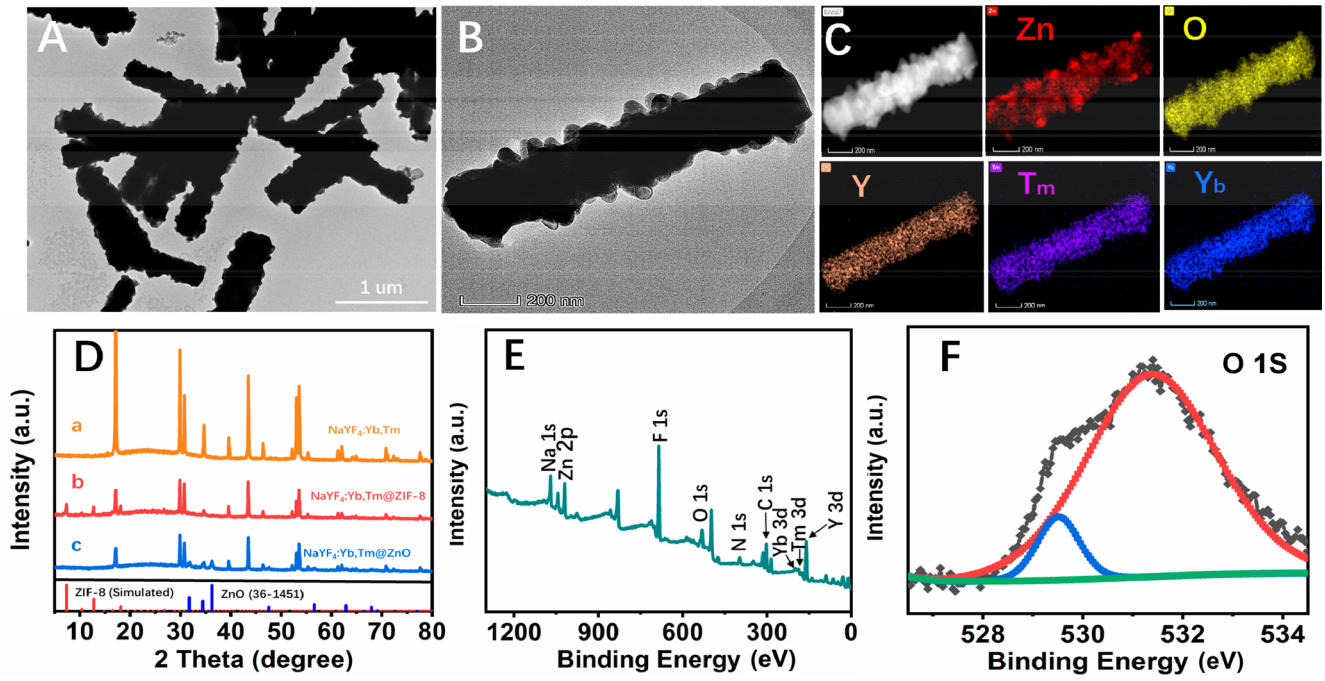

Figure 2. (A,B) TEM images of the $NaYF_4$:Yb,Tm@ZnO, corresponding HAADF-STEM image and element mappings (C) for Zn (red), O (yellow), Y (orange), Yb (mazarine blue) and Tm (purple); (D) XRD patterns of (a) $NaYF_4$:Yb,Tm, (b) $NaYF_4$:Yb,Tm@ZIF-8, and (c) $NaYF_4$:Yb,Tm@ZnO microrods; XPS survey spectrum (E) of $NaYF_4$:Yb,Tm@ZnO microrods and corresponding (F) O 1s orbits.

calcined $NaYF_4$:Yb,Tm@ZIF-8 template. As seen from Figure 1C,D, the ZIF-8 layer was distributed on the surface of $NaYF_4$:Yb,Tm microrods. To further demonstrate the elemental distribution of the $NaYF_4$:Yb,Tm@ZIF-8, the energy dispersive spectrometry (EDS) element mappings analysis was carried out (Figure 1E). The coexistence and dispersion of Zn (red), N (wathet blue), Na (pink), F (green), Y (orange), Yb (mazarine blue), and Tm (purple) elements throughout the whole of the microrods, reflected the complete coverage of ZIF-8 on the surface of $NaYF_4$:Yb,Tm microrods. What's more, relative to pure $NaYF_4$:Yb,Tm (Figure 2D, curve a), the two new major diffraction peaks of the prepared $NaYF_4$:Yb,Tm@ZIF-8 in the powder X-ray diffraction (XRD) (Figure 2D, curve b) observed at 7.3°and 12.7° were ascribed to corresponded (011), and (112) planes of ZIF-8, further suggesting the successful assembly of ZIF-8 on $NaYF_4$:Yb,Tm surface.[31] Then, after calcining the $NaYF_4$:Yb,Tm@ZIF-8, the surface morphologies of the prepared $NaYF_4$:Yb,Tm@ZnO were as shown in Figure 2A,B.

First, the morphology of the $NaYF_4$:Yb,Tm@ZnO was obviously different from the $NaYF_4$:Yb,Tm@ZIF-8. The formed irregular ZnO particles, which were consistent with the reported literature,[29] consisted of the light response layer on the surface of the $NaYF_4$:Yb,Tm microrods. The corresponding HAADF-STEM image of $NaYF_4$:Yb,Tm@ZnO and element mappings (Figure 2C) for Zn (red), O (yellow), Y (orange), Yb (mazarine blue), and Tm (purple) could be preliminary evidence that ZnO uniformly grew on the surface of $NaYF_4$:Yb,Tm. Furthermore, the crystal structure of the $NaYF_4$:Yb,Tm@ZnO was indexed to the standard XRD pattern of $NaYF_4$:Yb,Tm (PDF No. 28−1192) (Figure 2D, curve a) and ZnO (PDF No. 36−1451) (Figure 2D, curve c), indicating the ZnO was formed. Subsequently, X-ray photoelectron spectroscopy (XPS) was applied to analyze the chemical composition and status. The full XPS survey spectrum (Figure 2E) of $NaYF_4$:Yb,Tm@ZnO revealed the presence of Na, Y, F, Yb, Tm, Zn, C, N, O in composite. O 1s XPS of the $NaYF_4$:Yb,Tm@ZnO were fitted into two peaks located at 531.4 and 529.5 eV (Figure 2F). The binding energy at 531.4 eV was assigned to hydroxyl radicals (H−O), whereas the binding energy at 529.5 eV derived from O^{2-} ions of Zn−O bonds in wurtzite structure with Zn^{2+} in hexagonal coordination,[29,32] further indicating the formation of ZnO. The successful preparation of $NaYF_4$:Yb,Tm@ZnO provided a necessary condition for the development of NIR light-mediated PEC biosensor.

Feasibility of the NIR Light-Mediated PEC Biosensor. In this work, ZIF-8-assisted $NaYF_4$:Yb,Tm@ZnO was employed as converter to transfer NIR import to photocurrent output: $NaYF_4$:Yb,Tm converted NIR excitation to high-energy UV by the upconversion process and the ZnO could absorb the produced UV to generate photocurrent. First, the emission and absorption relationship between the $NaYF_4$:Yb,Tm and ZnO could be proved via the fluorescence changes before and after the ZnO coating on the Yb^{3+},Tm^{3+}-doped $NaYF_4$ (Figure 3A). Upon the 980 nm NIR laser excitation, the Yb^{3+} as sensitizer could absorb the NIR light, while Tm^{3+} was utilized as activator to provide various emissions. The fluorescence emission peaks of $NaYF_4$:Yb,Tm located at 292, 346, and 363 nm were ascribed to $^1I_6 \rightarrow {}^3H_6$, $^1I_6 \rightarrow {}^3F_4$, and $^1D_2 \rightarrow {}^3H_6$ transitions of Tm^{3+}, respectively. Moreover, another Tm^{3+} transitions ($_1D^2 \rightarrow {}_3F^4$ and $_1G^4 \rightarrow {}_3H^6$) could also emit fluorescence at 453 and 479 nm[10] (Figure 3A, curve a). In contrast, when the ZnO was coated on the surface of $NaYF_4$:Yb,Tm, the emission intensity of the fluorescence performed an obvious deceleration (curve b), suggesting most of the UV light from $NaYF_4$:Yb,Tm was absorbed by ZnO. As for PEC detection, this NIR light-driven PEC biosensor was based on DNA walker for signal enhancement on the DNA 3D tracks. Therefore, the design

DOI: 10.1021/acs.analchem.9b04710
Anal. Chem. 2020, 92, 1470−1476

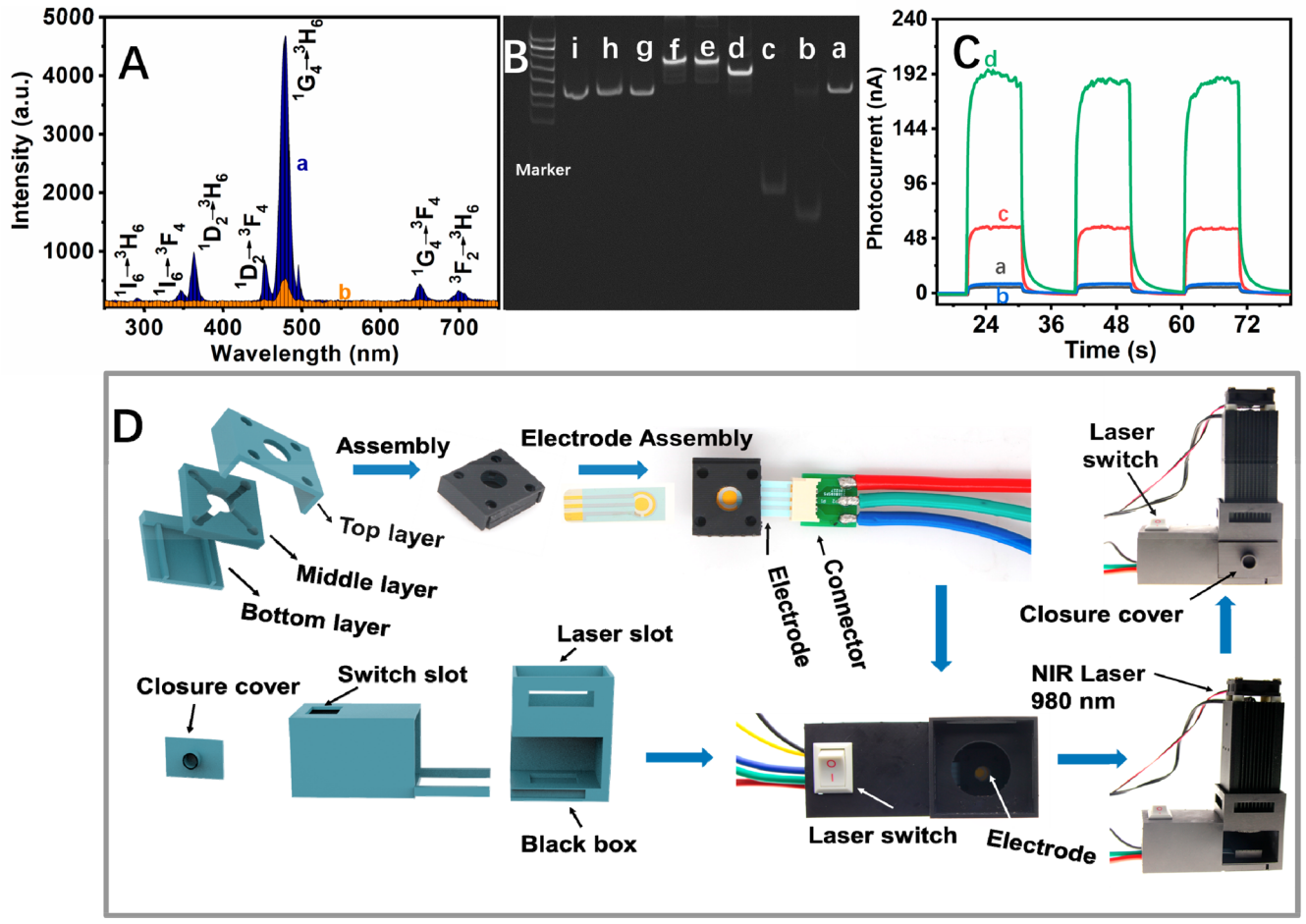

Figure 3. Upconversion photoluminescence (A) spectra of (a) $NaYF_4$:Yb,Tm and (b) $NaYF_4$:Yb,Tm@ZnO; (B) PAGE for different samples of DNA walker (marker: 300 bp; lanes a, swing arm DNA; lane b, anchorage DNA; lane c, blocker DNA; lane d, swing arm DNA + anchorage DNA; lane e, swing arm DNA + blocker DNA; lane f, swing arm DNA + blocker DNA+ anchorage DNA; lane g–i, the products after the lane d–f samples reacting with Exo III, respectively; (C) Photocurrent responses of (a) $NaYF_4$:Yb,Tm, (b) $NaYF_4$:Yb,Tm@ZIF-8, (c) $NaYF_4$:Yb,Tm@ZnO and (d) $NaYF_4$:Yb,Tm@ZnO toward 100 ng mL^{-1} CEA; (D) Photograph of homemade 3D model printed devices and assembly process.

of DNA walker for the release of guanine bases was crucial. To demonstrate the feasibility of the DNA walker strategy, native-polyacrylamide gel electrophoresis (PAGE) was carried out to monitor and contrast different products during the reaction process (Figure 3B). Lanes b and c gave shallow PAGE bands of single-strand anchorage DNA (lane b) and blocker DNA (lane c), respectively. It was clear that the length of two types of DNA strands were much smaller than those of the swinging arm DNA (lane a). In order to surmount the target-independent spontaneous hybridization between anchorage DNA and swing arm DNA, the blocker DNA sequence was designed longer than the anchorage DNA sequence, so that the complex product (line d) of anchorage DNA and swing arm DNA moved faster than the blocker DNA and swing arm DNA reaction product (line e). Correspondingly, when anchorage DNA was added into the blocked swing arm DNA (the complex product of the swing arm DNA and blocker DNA), the band (line f) of the blocked swing arm DNA was not influenced by the anchorage DNA (the band of blocker DNA could not be observed because of the blocker DNA's low content and short sequence), indicating the blocker DNA could prevent the target-independent spontaneous hybridization. Upon further addition of Exo III in the three products (lines d–f), another three bright bands of the newly released swing arm DNA from the above products could be observed (lanes g–i), which demonstrated that the swing arm DNA could get rid of blocker DNA and combine with anchorage DNA to release guanine bases with the digestion of Exo III. Next, the PEC detection was executed to analyze the photocurrent response of this strategy at different stages on a homemade 3D printed device containing six parts (SI Figure S2) and the assembly process could be observed from Figure 3D. The final detection results showed that $NaYF_4$:Yb,Tm-based electrode performed very weak photocurrent (Figure 3C, curve a) and the photocurrent decreased after the ZIF-8 assembling on the surface of the $NaYF_4$:Yb,Tm due to the poor conductivity of ZIF-8 (curve b). However, the photocurrent of $NaYF_4$:Yb,Tm@ZnO had a sharp increase under ZnO photosensitive properties (curve c). The photocurrent response of PEC sensing platform toward target CEA (100 ng mL^{-1} used as an example) was further explored. The obvious increases in photocurrent signals were observed (curve d), which attributed to the fact that the released guanine bases from the digestion of Exo III in the DNA walker process suppressed the electron–hole recombination of ZnO. All these results revealed that the developed NIR light-mediated PEC biosensor for the detection of CEA was feasible.

DOI: 10.1021/acs.analchem.9b04710
Anal. Chem. 2020, 92, 1470–1476

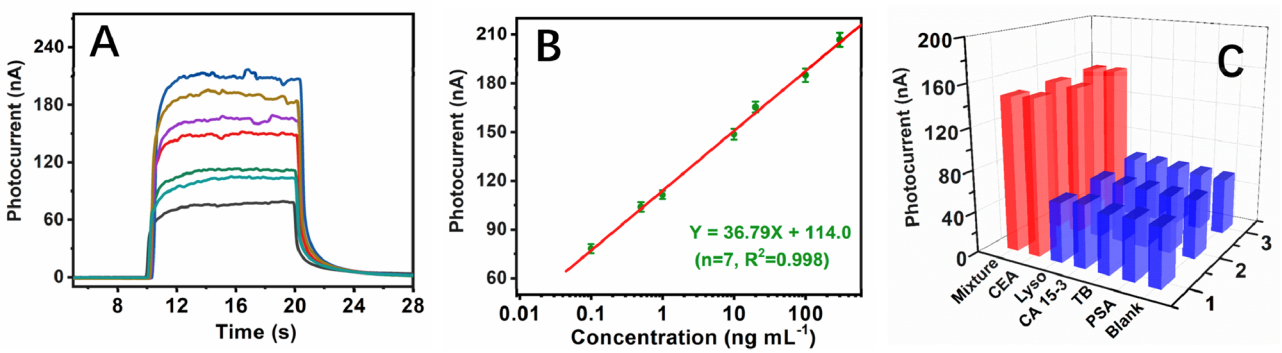

Figure 4. (A) Photocurrent responses of $NaYF_4$:Yb,Tm@ZnO-based PEC biosensor toward different CEA concentrations; (B) The corresponding linear relationship; (C) Selectivity of $NaYF_4$:Yb,Tm@ZnO-based PEC biosensor toward CEA (10 ng mL^{-1}), TB (100 ng mL^{-1}), PSA (100 ng mL^{-1}), Lyso (100 ng mL^{-1}), CA 15−3 (100 ng mL^{-1}), and the mixture containing the above-mentioned analytes. Note: Each data point represents the average value obtained from three different measurements with various biosensors, and the error bars represent the 95% confidence of the mean of the photocurrents.

Optimization of Experimental Conditions. As mentioned above, some crucial experimental conditions such as the incubation time of CEA-aptamer and reaction time of DNA walker with the Exo III actuation were investigated to obtain optimal analytical performance. In general, the binding between CEA and aptamer (partial fragment of swing arm DNA) triggered the enablement of DNA walker, which influenced the response of photocurrent directly. SI Figure S3A displays the changes of photocurrent signals toward different CEA-aptamer incubation time. The photocurrent responses gradually increased and reached the platform at 60 min. Therefore, 60 min was sufficient for CEA to combine with its aptamer. On the other hand, in the process of DNA walker, the digestion of Exo III toward DNA complex deriving from the combination of swing arm DNA and anchorage DNA could influence the quantity of the released guanines. Apparently, as seen in SI Figure S3B, the highest photocurrent appeared when the reaction time of DNA walker reached 110 min. Thus, in order to save sensing time, 110 min was selected as the reaction time for the DNA walker under the digestion of Exo III.

Analytical Performance of NIR Light-Mediated PEC Biosensor. By combining ZIF-8-assisted $NaYF_4$:Yb,Tm@ZnO with DNA walker on the 3D track for PEC sensing platform, a series of CEA standards with various concentrations were systematically detected under optimized reaction circumstances with NIR light irradiation to assess the analytical performance. Figure 4A exhibits the photocurrent signals responses toward target CEA. The responses of the photocurrent gradually increased with increasing CEA concentration over the range from 0.1 ng mL^{-1} to 300 ng mL^{-1}. The corresponding linear regression equation was y (nA) = 114.0 + 36.79 × $\log C_{[CEA]}$ (ng mL^{-1}) (R^2 = 0.998, n = 7) with the limit of detection (LOD) of 0.032 ng mL^{-1}. In fact, the selectivity of the detection platform was crucial due to the presence of interfering proteins in human serums such as thrombin (TB), prostate-specific antigen (PSA), lysozyme (Lyso), and cancer antigen 15−3 (CA 15−3). Therefore, the above interfering proteins were employed to evaluate the selectivity of the PEC biosensor. It was found that the photocurrent response of each interfering protein (100 ng mL^{-1}) was basically consistent with the blank value even if their concentrations were increased to 10 times that of the target CEA (10 ng mL^{-1}). Furthermore, the mixture (including all interfering proteins and target CEA) had an almost uniformly strong photocurrent response compared with target CEA, proving the satisfactory antijamming ability toward interfering proteins. Moreover, the accuracy of the $NaYF_4$:Yb,Tm@ZnO-based PEC biosensor triggered by NIR was evaluated by sensing six human serum specimens and comparing them with a commercial CEA-ELISA diagnostic kit at the same time. Carefully, all tools used during the measurements in contact with patient specimens were thoroughly disinfected. The final results are shown in SI Table S1. The accuracy of this strategy was investigated by a t-test method.[33−35] All t_{exp} values were below 2.77 ($t_{crit[0.05,4]}$ = 2.77), indicating no significant differences between the two methods and great accuracy for the CEA detection in human serum specimens.

CONCLUSIONS

In summary, this work developed a novel $NaYF_4$:Yb,Tm@ZnO-based PEC biosensor for CEA determination assisted by DNA walker with a homemade 3D printed device. The 3D printed device employed in this work miniaturizes the detection equipment of a cancer biomarker, assembles easily, and accomplishes portable detection. By means of a ZIF-8 template, ZnO was uniformly covered on the surface of $NaYF_4$:Yb,Tm by calcining, so that ZnO can be excited in situ by ultraviolet light from $NaYF_4$:Yb,Tm to generate photocurrent, extending the application of MOF-derived photoelectric materials. In addition, the 3D tracks of DNA walker with powerful enrichment ability enhance the PEC signal responses and increase the sensitivity of the detection platform. Moreover, the NIR light source can maintain strong penetration depth as well as near-zero photobleaching during the process of PEC measurement. Therefore, the UCNPs-based PEC biosensor driven by NIR light with the merits of high sensitivity and selectivity offers a reliable mechanism for CEA detection. Nevertheless, the limitations of this strategy still exist such as tedious biological assembly process, facilitating the improvement of our next work in terms of microminiaturization, portability, and simplification.

ASSOCIATED CONTENT

Supporting Information

The Supporting Information is available free of charge at https://pubs.acs.org/doi/10.1021/acs.analchem.9b04710.

DOI: 10.1021/acs.analchem.9b04710
Anal. Chem. 2020, 92, 1470−1476

Measurement with CEA ELISA kit for human serum samples, calculation method for *t*-test statistics, Figure S1−S3 (PDF)

AUTHOR INFORMATION

Corresponding Author

*Phone: +86-591-2286 6125. Fax: +86-591-2286 6135. E-mail: dianping.tang@fzu.edu.cn.

ORCID

Dianping Tang: 0000-0002-0134-3983

Notes

The authors declare no competing financial interest.

ACKNOWLEDGMENTS

We acknowledge financial support from the National Natural Science Foundation of China (21675029, 201874022) and the Health-Education Joint Research Project of Fujian Province (WKJ2016-2-15).

REFERENCES

(1) Yang, B.; Wang, Y.; Wei, T.; Pan, Y.; Zhou, E.; Yuan, Z.; Han, Y.; Li, M.; Ling, X.; Yin, L.; Xie, X.; Huang, L. *Adv. Funct. Mater.* **2018**, *28*, 1801782−1801789.

(2) Wang, L.; Guo, S.; Liu, D.; He, J.; Zhou, J.; Zhang, K.; Wei, Y.; Pan, Y.; Gao, C.; Yuan, Z.; Lei, D.; Xie, X.; Huang, L. *Adv. Funct. Mater.* **2019**, *29*, 1901242−1901252.

(3) Sun, L.; Wang, Y.; Yan, C. *Acc. Chem. Res.* **2014**, *47*, 1001−1009.

(4) Han, S.; Samanta, A.; Xie, X.; Huang, L.; Peng, J.; Park, S.; Teh, D.; Choi, Y.; Chang, Y.; All, A.; Yang, Y.; Xing, B.; Liu, X. *Adv. Mater.* **2017**, *29*, 1700244−1700251.

(5) Chen, J.; Zhao, J. *Sensors* **2012**, *12*, 2414−2435.

(6) Wu, Q.; Chen, H.; Fang, A.; Wu, X.; Liu, M.; Li, H.; Zhang, Y.; Yao, S. *ACS Sens.* **2017**, *2*, 1805−1813.

(7) Guan, Y.; Lu, H.; Li, W.; Zheng, Y.; Jiang, Z.; Zou, J.; Gao, H. *ACS Appl. Mater. Interfaces* **2017**, *9*, 26731−26739.

(8) Chen, X.; Xu, W.; Jiang, Y.; Pan, G.; Zhou, D.; Zhu, J.; Wang, H.; Chen, C.; Li, D.; Song, H. *Nanoscale* **2017**, *9*, 16357−16364.

(9) Luo, Z.; Qi, Q.; Zhang, L.; Zeng, R.; Su, L.; Tang, D. *Anal. Chem.* **2019**, *91*, 4149−4156.

(10) Qiu, Z.; Shu, J.; Tang, D. *Anal. Chem.* **2018**, *90*, 1021−1028.

(11) Qiu, Z.; Shu, J.; Liu, J.; Tang, D. *Anal. Chem.* **2019**, *91*, 1260−1268.

(12) Li, M.; Zheng, Z.; Zheng, Y.; Cui, C.; Li, C.; Li, Z. *ACS Appl. Mater. Interfaces* **2017**, *9*, 2899−2905.

(13) Guan, B.; Kushima, A.; Yu, L.; Li, S.; Li, J.; Lou, X. *Adv. Mater.* **2017**, *29*, 1605902−1605910.

(14) Hu, H.; Zhang, J.; Guan, B.; Lou, X. *Angew. Chem., Int. Ed.* **2016**, *55*, 9514−9518.

(15) Guan, B.; Yu, L.; Wang, X.; Song, S.; Lou, X. *Adv. Mater.* **2017**, *29*, 1605051−1605056.

(16) Tang, J.; Salunkhe, R.; Liu, J.; Torad, N.; Imura, M.; Furukawa, S.; Yamauchi, Y. *J. Am. Chem. Soc.* **2015**, *137*, 1572−1580.

(17) Zhang, S.; Guan, B.; Wu, H.; Lou, X. *Nano-Micro Lett.* **2018**, *10*, 70−78.

(18) Wu, R.; Wang, D.; Rui, X.; Liu, B.; Zhou, K.; Law, A.; Yan, Q.; Wei, J.; Chen, Z. *Adv. Mater.* **2015**, *27*, 3038−3044.

(19) Bennett, T.; Cao, S.; Tan, J.; Keen, D.; Bithell, E.; Beldon, P.; Friscic, T.; Cheetham, A. *J. Am. Chem. Soc.* **2011**, *133*, 14546−14549.

(20) Wang, C.; Wang, L.; Tadepalli, S.; Morrissey, J.; Kharasch, E.; Naik, R.; Singamaneni, S. *ACS Sens.* **2018**, *3*, 342−351.

(21) Zeng, Z.; Fang, X.; Miao, W.; Liu, Y.; Maiyalagan, T.; Mao, S. *ACS Sens.* **2019**, *4*, 1934−1941.

(22) Lai, L.; Yeong, Y.; Lau, K.; Shariff, A. *Chem. Eng. Technol.* **2017**, *40*, 1031−1042.

(23) Zhuang, J.; Kuo, C.; Chou, L.; Liu, D.; Weerapana, E.; Tsung, C. *ACS Nano* **2014**, *8*, 2812−2819.

(24) Wang, Z.; Elbaz, J.; Willner, I. *Nano Lett.* **2011**, *11*, 304−309.

(25) Yang, X.; Tang, Y.; Mason, S.; Chen, J.; Li, F. *ACS Nano* **2016**, *10*, 2324−2330.

(26) Jung, C.; Allen, P.; Ellington, A. *ACS Nano* **2017**, *11*, 8047−8054.

(27) Zhang, H.; Lai, M.; Zuehlke, A.; Peng, H.; Li, X.; Le, X. *Angew. Chem., Int. Ed.* **2015**, *54*, 14326−14330.

(28) Qu, X.; Zhu, D.; Yao, G.; Su, S.; Chao, J.; Liu, H.; Zuo, X.; Wang, L.; Shi, J.; Wang, L.; Huang, W.; Pei, H.; Fan, C. *Angew. Chem., Int. Ed.* **2017**, *56*, 1855−1858.

(29) Pan, L.; Muhammad, T.; Ma, L.; Huang, Z.; Wang, S.; Wang, L.; Zou, J.; Zhang, X. *Appl. Catal., B* **2016**, *189*, 181−191.

(30) Li, W.; Wang, L.; Jiang, W. *Chem. Commun.* **2017**, *53*, 5527−5530.

(31) Drobek, M.; Kim, J.; Bechelany, M.; Vallicari, C.; Julbe, A.; Kim, S. *ACS Appl. Mater. Interfaces* **2016**, *8*, 8323−8328.

(32) Chen, M.; Wang, X.; Yu, Y.; Pei, Z.; Bai, X.; Sun, C.; Huang, R.; Wen, L. *Appl. Surf. Sci.* **2000**, *158*, 134−140.

(33) Lv, S.; Zhang, K.; Zeng, Y.; Tang, D. *Anal. Chem.* **2018**, *90*, 7086−7093.

(34) Zeng, R.; Luo, Z.; Su, L.; Zhang, L.; Tang, D.; Niessner, R.; Knopp, D. *Anal. Chem.* **2019**, *91*, 2447−2454.

(35) Yu, Z.; Tang, Y.; Cai, G.; Ren, R.; Tang, D. *Anal. Chem.* **2019**, *91*, 1222−1226.

DOI: 10.1021/acs.analchem.9b04710
Anal. Chem. 2020, 92, 1470−1476